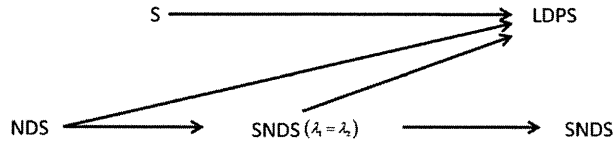

Fig. 1. Relationship among models. *Note*: $M_1 \rightarrow M_2$ indicates that model M_2 implies model M_1.

Let X and Y denote the row and column variables, respectively. Under the SNDS model, we see

$$\frac{p_{ij}}{p_{ji}} = \left(\alpha_2^2\right)^{i-j} \mu_{ij} \quad (i < j),$$

where

$$\mu_{ij} = \frac{\Phi(i\lambda_1 + j\lambda_2)}{\Phi(j\lambda_1 + i\lambda_2)}.$$

Note that only when $\lambda_1 = \lambda_2$, this structure is analogous to the LDPS structure. When $\lambda_1 = \lambda_2$, the SNDS model is a special case of the LDPS model. So, we also propose the SNDS model with $\lambda_1 = \lambda_2$ as the special SNDS model. For the special SNDS model, see Section 3. Under the SNDS model, if all $\{(\alpha_2^2)^{i-j}\mu_{ij} > 1\}$ hold, then $\Pr(X \leq i) > \Pr(Y \leq i)$, $i = 1, \ldots, r-1$, hold. In addition, (1) if $\alpha_1, \beta_1, \beta_2 > 1$, $\alpha_2 < 1$ and $\lambda_2 > 0$, p_{ij} increases as the column value j increases, when the row value i is fixed, and (2) if $\alpha_1, \alpha_2, \beta_1, \beta_2 > 1$ and $\lambda_1 > 0$, p_{ij} increases as the row value i increases, when the column value j is fixed.

In addition, since the SNDS model is expressed by multiplying the form of the NDS model by cumulative distribution function of standard normal $\Phi(i\lambda_1 + j\lambda_2)$, we can consider the generalization of the SNDS model as follows:

$$p_{ij} = 2\xi\alpha_1^{(i-j)^2}\alpha_2^{i-j}\beta_1^{(i+j)^2}\beta_2^{i+j}F(i\lambda_1 + j\lambda_2) \quad (i = 1, \ldots, r; j = 1, \ldots, r),$$

where $F(\cdot)$ is the strictly increasing function with $0 < F(\cdot) < 1$. We shall refer to this model as the generalized NDS (GNDS) model. For the details of discussions using GNDS model, see Section 3.

Fig. 1 shows the relationship among the models considered here.

2.2. Goodness-of-fit test

We describe a goodness-of-fit test for a proposed model, named SNDS, in the previous section. Let n_{ij} denote the observed frequency in the (i, j)th cell of the table ($i = 1, \ldots, r; j = 1, \ldots, r$) and let m_{ij} denote the corresponding expected frequency. Assuming that $\{n_{ij}\}$ have a multinomial distribution, the maximum likelihood estimates (MLEs) of expected frequencies $\{m_{ij}\}$ under the SNDS model could be obtained by maximizing the kernel of the log-likelihood function, subject to the constraint $\sum\sum p_{ij} = 1$, using the method of Lagrange multiplier. Namely, we must maximize the following function with respect to $\{p_{ij}\}$, λ and $\{\phi_{ij}\}$:

$$\sum_{i=1}^{r}\sum_{j=1}^{r} n_{ij}\log p_{ij} - \lambda\left(\sum_{i=1}^{r}\sum_{j=1}^{r} p_{ij} - 1\right) - \sum_{i=1}^{r}\sum_{j=1}^{r}\phi_{ij}\left(p_{ij} - 2\xi\alpha_1^{(i-j)^2}\alpha_2^{i-j}\beta_1^{(i+j)^2}\beta_2^{i+j}\Phi(i\lambda_1 + j\lambda_2)\right).$$

Then, using the Newton–Raphson method, we can obtain the MLEs of $\{m_{ij}\}$ and parameters $\xi, \alpha_1, \alpha_2, \beta_1, \beta_2, \lambda_1, \lambda_2$ under the SNDS model.

The likelihood ratio chi-squared statistic for testing goodness-of-fit of a model symbolized by M is

$$G^2 = 2\sum_{i=1}^{r}\sum_{j=1}^{r} n_{ij}\log\left(\frac{n_{ij}}{\hat{m}_{ij}}\right),$$

where $\hat{m}_{ij}$ is the MLE of m_{ij} under the model M. The numbers of degrees of freedom (df) for the LDPS, NDS and SNDS models are $(r-2)(r+1)/2$, $r^2 - 5$, and $r^2 - 7$, respectively.

3. Simulation studies

We present our investigation of the behavior of the new model for a bivariate skew normal distribution. Let the random variable $\boldsymbol{Z} = (Z_1, Z_2)^T$ be distributed as a bivariate skew normal distribution with the density like Eq. (2). Suppose that there is an underlying bivariate skew normal distribution with some conditions and suppose that a 4×4 table is formed using cutpoints for each variable at -0.6, 0 and 0.6. Then, in terms of simulation studies, each subtable of Table 1 gives a 4×4 table of sample size 10 000, formed from an underlying bivariate skew normal distribution with various location, scale and skew parameters. Especially, in Table 1(a) and (b), there is an underlying bivariate skew normal distribution with skew parameters γ_1 and γ_2 being zero; i.e., there is an underlying bivariate normal distribution.

We see from Table 2(a) that both the NDS and SNDS models fit the data in Table 1(a) and (b) well. This seems natural because there is an underlying bivariate normal distribution in Table 1(a) and (b).

Table 1
The 4×4 tables of sample size 10 000, formed by using cutpoints for each variable at -0.6, 0 and 0.6 from an underlying bivariate skew normal distribution with various conditions.

(a) $\mu_1 = \mu_2 = 0, \sigma^2 = 1, \rho = 0.3, \gamma_1 = \gamma_2 = 0$				(b) $\mu_1 = 0.1, \mu_2 = 0.2, \sigma^2 = 1.5, \rho = 0.5, \gamma_1 = \gamma_2 = 0$			
1137	685	536	390	1090	597	510	683
704	559	512	514	500	329	341	589
540	504	519	679	446	346	397	758
432	491	696	1102	478	494	691	1751
(c) $\mu_1 = \mu_2 = 0, \sigma^2 = 1, \rho = 0.3, \gamma_1 = \gamma_2 = 0.3$				(d) $\mu_1 = \mu_2 = 0, \sigma^2 = 3, \rho = 0.3, \gamma_1 = \gamma_2 = 0.5$			
486	449	404	431	473	251	344	1165
432	447	481	678	290	155	177	670
415	520	599	919	353	182	217	805
419	660	961	1699	1155	651	735	2377
(e) $\mu_1 = \mu_2 = 0.1, \sigma^2 = 2, \rho = 0.3, \gamma_1 = \gamma_2 = 0.3$				(f) $\mu_1 = \mu_2 = -0.1, \sigma^2 = 2, \rho = 0.3, \gamma_1 = \gamma_2 = 0.3$			
632	348	410	900	758	487	476	930
329	205	251	694	446	264	270	569
386	254	295	791	435	290	292	706
864	633	767	2241	998	626	686	1767
(g) $\mu_1 = 0, \mu_2 = 0.2, \sigma^2 = 2, \rho = 0.3, \gamma_1 = \gamma_2 = 0.3$				(h) $\mu_1 = \mu_2 = 0, \sigma^2 = 2, \rho = 0.3, \gamma_1 = 0.1, \gamma_2 = 0.3$			
560	390	448	1092	836	484	558	1092
317	209	254	701	415	262	274	662
324	259	316	817	400	270	289	680
755	560	709	2289	785	549	659	1785
(i) $\mu_1 = 0.1, \mu_2 = 0.2, \sigma^2 = 2, \rho = 0.3, \gamma_1 = 0.1, \gamma_2 = 0.3$				(j) $\mu_1 = 0.1, \mu_2 = 0.2, \sigma^2 = 2, \rho = 0.3, \gamma_1 = 0.3, \gamma_2 = -0.3$			
676	437	527	1136	1137	403	344	559
343	225	259	699	575	278	242	438
359	240	293	779	576	293	283	528
677	531	687	2132	1213	733	740	1658

Table 2
The values of likelihood ratio chi-squared statistic G^2 for (a) the SNDS and NDS models, and (b) the GNDS model with some cumulative distribution functions, applied to the data in Table 1.

(a) G^2 for the SNDS and NDS models

Tables	G^2(SNDS)	G^2(NDS)
Table 1(a)	8.28	9.02
Table 1(b)	12.53	13.53
Table 1(c)	15.73	20.22*
Table 1(d)	12.93	20.73*
Table 1(e)	13.06	19.79*
Table 1(f)	13.15	22.59*
Table 1(g)	14.35	20.01*
Table 1(h)	12.90	20.50*
Table 1(i)	12.85	20.35*
Table 1(j)	16.11	20.03*

(b) G^2 for the GNDS model with the logistic, Cauchy and exponential distribution function

Tables	G^2(GNDS) (logistic)	G^2(GNDS)(Cauchy)	G^2(GNDS)(exponential)
Table 1(a)	8.36	8.50	6.12
Table 1(b)	12.81	12.73	13.53
Table 1(c)	15.63	15.81	15.58
Table 1(d)	13.19	13.72	13.03
Table 1(e)	19.05*	13.51	19.05*
Table 1(f)	14.30	16.65	10.59
Table 1(g)	15.10	16.49	13.89
Table 1(h)	13.35	14.43	12.01
Table 1(i)	13.53	15.02	10.54
Table 1(j)	16.31	16.94*	18.86*

* Means significant at the 0.05 level.

On the other hand, in Table 1(c) to (j) there is an underlying bivariate skew normal distribution with skew parameters γ_1 and γ_2 being non-zero. Then, we see from Table 2(a) that the SNDS model fits all the data in from Table 1(c) to (j) well, but the NDS model fits them poorly. Therefore, the SNDS model is more appropriate for a square contingency table if it is reasonable to assume an underlying bivariate skew normal distribution with equal marginal variances.

Table 3
Decayed teeth data of 349 men aged 18–39, for patients visiting a dental clinic in Sapporo City, Japan, from 2001 to 2005 (Tomizawa et al., 2006). (The parenthesized values are MLEs of expected frequencies under the SNDS model.)

Lower (numbers of decayed teeth)	Upper (numbers of decayed teeth)			Total
	0–4 (1)	5–8 (2)	9+ (3)	
0–4 (1)	115 (110.23)	55 (60.89)	25 (23.97)	195
5–8 (2)	16 (21.23)	49 (45.84)	60 (57.74)	125
9+ (3)	1 (0.45)	7 (4.46)	21 (24.19)	29
Total	132	111	106	349

Table 4
The values of likelihood ratio chi-squared statistic G^2 for models applied to the data in Table 3.

Models	df	G^2
Symmetry	3	98.24*
LDPS	2	3.72
NDS	4	20.17*
Special SNDS	3	20.17*
SNDS	2	4.72

* Means significant at the 0.05 level.

Next, we shall apply the GNDS model with $F(\cdot)$ to Table 1. Then we set the standard logistic and standard Cauchy distributions as the symmetric distribution with respect to zero, and standard exponential distribution as not-symmetric distribution, for the cumulative function $F(\cdot)$. We see from Table 2(b) that the GNDS models with the standard logistic and standard Cauchy distribution functions fit all the subtables in Table 1 well, and the values of G^2(GNDS) are very close to the values G^2(SNDS). This is because standard normal distribution function is similar to the standard logistic and standard Cauchy distribution functions. For the GNDS model with standard exponential distribution, the values of G^2 for the GNDS model are not different from the G^2 for the SNDS model so much. The GNDS model is an extension of the NDS model, and so the values of G^2 for the GNDS model are less than those for the NDS model. In addition, the term $F(\cdot)$ in the GNDS model may not be so different from the term $\Phi(\cdot)$ in the SNDS model, although standard normal distribution function itself is not similar to standard exponential distribution at all. It is thought that this is why the result described above is caused.

4. Analysis of decayed teeth data

We illustrate the techniques by applying the model of Section 2 to a real data by Tomizawa et al. (2006). The data are constructed from the data of the decayed teeth of 349 men aged 18–39, for the patients visiting a dental clinic in Sapporo City, Japan, from 2001 to 2005. Table 3 is classified by the number of decayed teeth on the lower side of the mouth of a patient and those on the upper side.

Table 4 gives the values of G^2 for models applied to the data in Table 3. We see from Table 4 that the NDS model fits the data poorly, on the other hand, the LDPS model fits them well. Thus we can guess that there is not an underlying normal distribution in Table 3, because both the NDS and LDPS models fit them well if there is an underlying normal distribution in the table. By the way, the SNDS model fits these data well, although the special SNDS model fits them poorly. So we shall investigate the data in Table 3 in more details using the SNDS model.

Under the SNDS model, the values of MLEs of parameters are $\hat{\alpha}_1 = 0.98, \hat{\alpha}_2 = 4.54, \hat{\beta}_1 = 1.09, \hat{\beta}_2 = 0.69, \hat{\lambda}_1 = -1.62, \hat{\lambda}_2 = 0.89$. So, we see $\{(\hat{\alpha}_2^2)^{i-j}\hat{\mu}_{ij} > 1\}$; i.e., $\Pr(X \le i) > \Pr(Y \le i)$, $i = 1, \ldots, r-1$. Therefore, the number of decayed teeth in the upper side of the mouth of a patient tends to be more than that in the lower side.

5. Discussions

The existing NDS model may be appropriate for a square ordinal table if it is reasonable to assume an underlying *bivariate normal distribution* with equal marginal variances. On the other hand, the proposed model, i.e., the SNDS model may be appropriate for a square ordinal table if it is reasonable to assume an underlying *bivariate skew normal distribution* with equal marginal variances. Then note that the SNDS model is an extension of the NDS model. Therefore, for analyzing square contingency table data, it may be useful to apply the SNDS model to these data if it is not reasonable to assume an underlying bivariate normal distribution. Moreover, it is meaningful to use the SNDS model even if it is reasonable to assume an underlying bivariate normal distribution, because the SNDS model implies the NDS model, which may be appropriate when assuming an underlying bivariate normal distribution.

Finally, we note that we cannot always consider that there is an underlying bivariate skew normal distribution even if the SNDS model fits data well (also see Section 3).

Acknowledgments

We are grateful to the editor and two anonymous reviewers for comments and suggestions which have led to improvement in this paper.

References

Agresti, A., 1983. A simple diagonals-parameter symmetry and quasi-symmetry model. Statist. Probab. Lett. 1, 313–316.
Azzalini, A., Dalla Valle, A., 1996. The multivariate skew-normal distribution. Biometrika 83, 715–726.
Baghfalaki, T., Ganjali, M., 2011. An EM estimation approach for analyzing bivariate skew normal data with non monotone missing values. Comm. Statist. Theory Methods 40, 1671–1686.
Bishop, Y.M.M., Fienberg, S.E., Holland, P.W., 1975. Discrete Multivariate Analysis: Theory and Practice. The MIT Press, Cambridge.
Bowker, A.H., 1948. A test for symmetry in contingency tables. J. Amer. Statist. Assoc. 43, 572–574.
Tahata, K., Tomizawa, S., 2010. Double linear diagonals-parameter symmetry and decomposition of double symmetry for square tables. Stat. Methods Appl. 19, 307–318.
Tahata, K., Yamamoto, K., Tomizawa, S., 2009. Normal distribution type symmetry model for square contingency tables with ordered categories. Open Statist. Probab. J. 1, 32–37.
Tomizawa, S., 1991. An extended linear diagonals-parameter symmetry model for square contingency tables with ordered categories. Metron 49, 401–409.
Tomizawa, S., Miyamoto, N., Iwamoto, M., 2006. Linear column-parameter symmetry model for square contingency tables: application to decayed teeth data. Biom. Lett. 43, 91–98.
Yamamoto, H., Iwashita, T., Tomizawa, S., 2007. Decomposition of symmetry into ordinal quasi-symmetry and marginal equimoment for multi-way tables. Austral. J. Statist. 36, 291–306.
Yamamoto, K., Kurakami, H., Iwashita, T., Tomizawa, S., 2008. Contaminated normal type symmetry model and decomposition of symmetry for square contingency tables. J. Stat. Theory Pract. 2, 651–661.

DOI: 10.3727/096368914X685799

CT-1353 Accepted 12/20/2014 for publication in "Cell Transplantation"

Functional and Electrical Integration of Induced Pluripotent Stem Cell-Derived Cardiomyocytes in a Myocardial Infarction Rat Heart

Short title: Integration of iPSC-cardiomyocytes in the heart

Takahiro Higuchi[1], MD, Shigeru Miyagawa MD, PhD[1], James T. Pearson, PhD[2,3], Satsuki Fukushima MD, PhD[1], Atsuhiro Saito PhD[4], Hirotsugu Tsuchimochi, PhD[5], Takashi Sonobe, PhD[4], Yutaka Fujii, MS[5], Naoto Yagi, PhD[6], Alberto Astolfo, PhD[2], Mikiyasu Shirai, MD PhD[5], Yoshiki Sawa MD, PhD[1]

[1]Department of Cardiac Surgery, Osaka University Graduate School of Medicine, Osaka, Japan, [2]The Australian Synchrotron, Clayton, Victoria Australia, [3]Monash Biomedical Imaging Facility, Monash University, Clayton, Victoria, Australia, [4]Medical Center for Translational Research, Osaka University Hospital, Osaka, Japan, [5]Department of Cardiac Physiology, National Cerebral and Cardiovascular Center Research Institute, Suita, Osaka, Japan, [6]SPring-8/JASRI, Sayo, Hyogo, Japan

Address for Correspondence; Professor Yoshiki Sawa

Department of Cardiovascular Surgery, Osaka University Graduate School of Medicine

2-2 Yamadaoka, Suita, 565-0871 Japan

Telephone; +81668793154, Facsimile; +81668793163

E-mail; sawa-p@surg1.med.osaka-u.ac.jp

Total word count: 5,328 words

CT-1353 Cell Transplantation Early Epub; provisional acceptance 12/04/2014

ABSTRACT

Functional and Electrical Integration of Induced Pluripotent Stem Cell-Derived Cardiomyocytes in a Myocardial Infarction Rat Heart

Higuchi T, Miyagawa S, Pearson JT, Fukushima S, Saito A, Tsuchimochi H, Sonobe T, Fujii Y,

In vitro expanded beating cardiac myocytes derived from induced pluripotent stem cells (iPSC-CMs) are a promising source of therapy for cardiac regeneration. Meanwhile, the cell-sheet method has been shown to potentially maximize survival, functionality and integration of the transplanted cells into the heart. It is thus hypothesized that transplanted iPSC-CMs in a cell-sheet manner may contribute to functional recovery *via* direct mechanical effects on the myocardial infarction (MI) heart.

: F344/NJcl-rnu/rnu rat were left coronary artery-ligated (n=30), followed by transplantation of Dsred-labeled iPSC-CMs cell-sheets of murine origin over the infarct heart surface. Effects of the treatment were assessed, including *in vivo* molecular/cellular evaluations using a synchrotron radiation scattering technique. Ejection fraction and activation recovery interval were significantly greater from day 3 onwards after iPSC-CMs transplantation compared to those after sham operation. A number of transplanted iPSC-CMs were present on the heart surface expressing cardiac myosin or connexin43 over two weeks, assessed by immunoconfocal microscopy, while mitochondria in the transplanted iPSC-CMs gradually showed mature structure as assessed by electronmicroscopy. Of note, X-ray diffraction identified 1,0 and 1,1 equatorial reflections attributable to myosin and actin-myosin lattice planes typical of organized cardiac muscle fibers within the transplanted cell-sheets at 4 weeks, suggesting cyclic systolic myosin mass transfer to actin filaments in the transplanted iPSC-CMs.

Transplantation of iPSC-CM cell-sheets into the heart yielded functional and electrical recovery with cyclic contraction of transplanted cells in the rat MI heart, indicating that this strategy may be a promising "cardiac muscle replacement" therapy.

Keywords: iPS cell; regeneration therapy; cell-sheet; synchrotron imaging

CT-1353 Cell Transplantation Early Epub; provisional acceptance 12/04/2014

INTRODUCTION

To increase the number of functional cardiomyocytes in the heart is a goal of regenerative therapy for advanced cardiac failure (14). It has been shown that induced pluripotent stem cells (iPSCs) differentiate into functional cardiomyocytes *in vitro* by specific culture regimens, suggesting that replacement of damaged cardiac tissue might be achieved by transplantation of iPSCs-derived cardiomyocytes (iPSC-CMs) into the damaged area using an appropriate cell-delivery method. Further, it has been shown that the cell-sheet method, in which a scaffold-free sheet-shaped cultured cell-cluster is placed on the surface of the heart, delivers a large number of the cells while preserving the functionality of the cells and the myocardium, indicating that the cell-sheet method may be an ideal delivery method of iPSC-CM to replace the damaged cardiac area (8,9,15). In fact, we reported that transplantation of iPSC-CMs into the heart by the cell-sheet method improves functional performance of the infarcted heart in pigs (5). However, in that study (5), synchronous contraction of the transplanted iPSC-CMs as "cardiac myocytes" that express the regular, cyclic actin-myosin cross-bridge motion, which is the aim of this treatment, was not demonstrated due to the limitations of current image analysis methods *in vivo*.

Shiba et al. reported that the fluorescent signal of calcium sensor, GCaMP3, which has been genetically encoded in the cells prior to transplantation into the heart, was useful for visualizing spontaneous contraction of the transplanted cells in the heart *in vivo* (16). However, the calcium sensor signal does not necessarily correlate with normal cyclic actin-myosin cross-bridge motion. On the other hand, third generation synchrotron radiation (SPring-8, Hyogo, Japan) has been utilized to quantify actin-myosin cross-bridge dynamics in cardiac fibres of localized regions *in vivo* (12,17). We herein hypothesized that transplanted iPSC-CMs in a cell-sheet manner may contribute to functional recovery *via* direct mechanical

CT-1353 Cell Transplantation Early Epub; provisional acceptance 12/04/2014

effects on myocardial infarction (MI) heart. We therefore explored functional and electrical integration of the transplanted iPSC-CMs in the acute MI rat heart using the latest imaging modality utilising synchrotron radiation from a third generation facility.

METHODS

Studies were performed with the approval of the ethics committee of Osaka University Graduate School of Medicine and the Animal Experiment Review Committee of the Japan Synchrotron Radiation Research Institute. All animals used in this study received care in compliance with the Guide for the Care and Use of Laboratory Animals (National Institutes of Health Publication No 85-23, revised 1996).

Cell-culture and cell-sheet generation

Germline-competent mouse iPSC-line 256H18 was established by introducing only *Oct3/4*, *Sox2*, and *Klf4* (without *c-Myc*), constitutively expressing red-fluorescent protein (Dsred) (generously contributed by Professor S Yamanaka, Kyoto University, Japan) (11). Maintenance of the 256H18 iPSCs and induction of cardiomyogenic differentiation was performed following the protocol established in Professor Yamanaka's and our laboratories, respectively (7,23). Briefly, the iPSCs were maintained on feeder layers of mitomycin C-treated mouse embryonic fibroblasts (Chemicon, Billerica, MA). Embryoid bodies (EBs) were then generated under the presence of 6-bromoindirubin-3′-oxime (Calbiochem, Darmstadt, Germany) (23).

The EBs were plated on 12-well temperature-responsive culture dishes (CellSeed, Tokyo, Japan) at 37°C with the EB number adjusted to 20 per well, thereafter the EBs were differentiated in the serum free medium with insulin-transferin-selenium-X (Invitrogen,

CT-1353 Cell Transplantation Early Epub; provisional acceptance 12/04/2014

Carlsbad, CA). Subsequently, the dishes were removed to refrigerator set at 20°C, while scaffold-free iPSC-CM cell-sheets detached spontaneously from the dish surfaces (23). Cardiac troponin T positivity in this preparation assessed by immunohistolabelling was consistently 70-80% (7,23).

Generation of acute myocardial infarction (MI) model and cell-sheet transplantation

Female F344/NJcl-rnu/rnu rats of 6 weeks of age (Crea, Tokyo, Japan) were anaesthetized by inhalation of isoflurane (1.5%) and endotracheally intubated for mechanical ventilation. The left coronary artery was then permanently occluded under thoracotomy (3). Two weeks after the ligation, the cell-sheet generated by iPSC-CMs or mitomycin C-treated mouse embryonic fibroblasts were simply placed on surface of the left ventricle (LV, n=6 each) (6). Bupivacaine (1% in saline, 250 μl) was subcutaneously injected near the incision line to minimize the postoperative pain and the rats were then recovered in a temperature-controlled individual cage.

Transthoracic echocardiography analysis

Transthoracic echocardiography was performed using a system equipped with a 12-MHz transducer and SONOS5500 (Agilent Technologies, Palo Alto, CA) under isoflurane inhalation (1%). Diastolic/systolic dimensions (Dd/Ds), and ejection fraction (EF) of the LV were measured (n=6 each) (3).

Telemetry study

A telemetry transmitter with two electrodes (Data Sciences International) was implanted prior to the treatment (day 14 post-MI) under inhalation of 1.5% isoflurane (n=4 each) (3). Electrocardiogram was then continuously monitored over 7 days. Ventricular premature

contractions (VPC) were detected and the frequency of the VPC was expressed as the number of VPC per day divided by the daily cumulative heart beats.

Electrical potential mapping analysis

Electrical potential mapping study was performed under the repeated left thoracotomies in the same animal at day 2, 3, 4, 7, and 14 (n=4 each group). There was no repeated procedures-related morbidity or mortality. A sixty-four electrical potential mapping system (Alpha MED Scientific, Osaka, Japan) was directly placed on surface of the LV *via* the thoracotomy under general anaesthesia and endotracheal intubation with mechanical ventilation as above. The electrical potential was recorded as the calculated activation recovery interval (ARI) in the same animals at the indicated time-points (n=4 each group).

Synchrotron small-angle scattering study

The fundamentals of synchrotron small-angle scattering techniques for the investigation of cross-bridge dynamics in the intact heart are presented in detail elsewhere (17). In brief, total thoracotomy was performed under general anaesthesia and endotracheal intubation with mechanical ventilation as above at the synchrotron radiation facility SPring-8 (n=4 in iPSC-CMs treated rats and in MI-only rats) as described in detail elsewhere (13). Cardiac catheterisation was performed to allow continuous LV pressure-volume recordings simultaneous with all SAXS and arterial pressure recordings. Pressure-volumetry was used to establish the timing of the cardiac cycle in all treatment periods and to permit assessment of actin-myosin contributions to global LV function. Heart rate (HR) was determined from the interval between end-diastolic (ED) events in the pressure-volume loops. Hemodynamic data were recorded using CHART (v5.5.6, ADInstruments, NSW) at a sampling rate of 1000/s.

A collimated quasi-monochromatic beam with 0.08 nm wavelength (15 keV),

dimensions 0.2 × 0.1mm (horizontal × vertical) and beam flux ~10^{12} photons/s (ring current 90–100 mA) was focused on the surface myocardium at an oblique tangent (rat ~3m from the detector). SAXS sequences (12 bit, 144 × 150 pixels) each lasting <2.1s were collected at a sampling interval of 15 ms with the aid of an image intensifier (V5445P, Hamamatsu Photonics, Hamamatsu, Japan) and a fast charge-coupled device camera (C4880-80-24A, Hamamatsu Photonics). Patterns were then digitally recorded using HiPic32 software (v5.1.0 Hamamatsu Photonics). With rats in a supine position, X-ray diffraction profiles were recorded vertically through the iPSC-CMs cell-sheet grafts and infarcted myocardium of the anterior LV wall of the exposed *in situ* beating hearts (12). Periodically between diffraction recordings a laser aligned with the X-ray beam was used to determine the point of path trajectory at which the beam also passed through normal myocardium. Diffraction patterns obtained from in situ iPSC sheets were of lower intensity compared to normal myocardium (remote regions) and easily distinguished on the basis of established cardiac fibre-intensity peak orientations (21).

Using custom software the average radial line profile around the centre of the spectrum was calculated using a three point background curve fitting process with manual definition of peak spectra limits. Background subtraction was then performed between user-defined inner and outer limits on either side of the 1,0 and 1,1 reflections. The integrated intensity of the 1,0 and 1,1 reflection intensities was then determined from the areas under the reflection peaks, defined as $I_{1,0}$ and $I_{1,1}$ respectively.

Enzyme-linked immunosorbent assay (ELISA)

Culture supernatants of cell-preparation were centrifuged to remove debris and cells. Content of vascular endothelial growth factor (VEGF) and hepatocyte growth factor (HGF) in the undiluted culture supernatants was determined with an ELISA kit (R&D Systems, MN, USA).

Immunohistolabelling analysis

Under anaesthesia by 5% isoflurane inhalation, heart was promptly excised, immersed in 4% paraformaldehyde, cut transversely and then frozen (n=5 each group). Ten μm-cryosections were labeled with monoclonal anti-cardiac myosin (Molecular Probes, Eugene, OR, USA), or monoclonal anti-connexin(Cx)43 (Millipore, Billerica, MA, USA) antibodies. The labelled sections were again labelled by the secondary antibodies (AlexaFluor488, or AlexaFluor594 phalloidin, Invitrogen), counterstained with 6-diamidino-2-phenylindole (DAPI, Invitrogen) and then assessed by immunoconfocal microscopy (FV1000D, Olympus, Tokyo, Japan)

Electron microscopy analysis

Sliced cardiac tissues were fixed with 2% glutaraldehyde in 0.1 mM phosphate buffer (pH 7.4) for 60 minutes at 4°C, washed and immersed overnight in PBS at 4°C, and fixed in 1% buffered osmium tetroxide, then dehydrated through graded ethanol and embedded in epoxy resin. Ultrathin sections (85 nm) were double-stained with uranyl acetate and lead citrate, and were observed under electron microscopy (H-7600; Hitachi, Tokyo, Japan).

Statistical analysis

All values were expressed as mean±standard deviations. Contents of VEGF and HGF in the supernatant of the four different cultures were compared by one-way ANOVA followed by Bonferroni's test for individual significant difference. Frequency of the VPC, ARI and LVEF were compared by two-way ANOVA followed by Bonferroni's tests for individual significant differences. $P < 0.05$ was considered to be statistically significant.

RESULTS

CT-1353 Cell Transplantation Early Epub; provisional acceptance 12/04/2014

iPSCs-derived cardiomyocytes as a source of potential paracrine effects

It has been shown that cell transplantation into the heart produces "paracrine effects", in which the transplanted cells release a variety of protective factors into the adjacent native cardiac tissue to enhance native regenerative process, such as neo-angiogenic, anti-fibrotic, or anti-apoptotic effects (2). Capacity to release protective factors, such as VEGF and HGF, which have been shown to be the most important factors in the paracrine effects, were investigated here *in vitro*. Supernatant of the culture dishes of iPSC-CMs and fibroblasts was collected to measure concentration of VEGF and HGF by ELISA, showing that concentration of VEGF and HGF was not significantly different in the conditioned medium of the iPSC-CMs and the fibroblasts, suggesting potential "paracrine effects" of the iPSC-CM transplantation therapy.

Electrical integrity and functional recovery after cell-sheet transplantation in vivo

Cell-sheet method has been shown to transplant abundant somatic-tissue derived cells into the heart, which can be integrated into the cardiac tissue with minimal damage to the transplanted cells and to the myocardium (9). Functional integration of cell-sheets generated by iPSC-CM into the heart is, however, poorly understood. We speculate that similarity of the phenotype and/or character of the iPSC-CM to the native CM might result in a better integration into the native cardiac tissue compared to somatic tissue-derived cells.

Scaffold-free cell-sheets generated by Dsred-labeled iPSC-CMs of mouse origin were transplanted into the nude rat heart that had been subjected to permanent occlusion of the left coronary artery prior to the cell-sheet transplantation. The cell-sheet generated by Dsred-labelled fibroblasts, were used as controls. Electrical integrity and arrhythmogenicity were assessed by daily Holter ECG monitoring and 64-channel electrical potential mapping. In addition, global cardiac function was serially assessed by transthoracic echocardiography.

CT-1353 Cell Transplantation Early Epub; provisional acceptance 12/04/2014

Electrical potential mapping identified multiple ectopic excitations over the cell-sheet transplanted area in the iPSC-CM group until day 2 (day 16 post-MI), which gradually disappeared from day 3 onwards (day 17 post-MI) (Figure 1A). In contrast, transplantation of the cell-sheet derived from fibroblasts, or MI-only rarely induced ectopic excitations over the study period. Ventricular premature contractions more frequently occurred post-iPSC-CM cell-sheet transplantation than those post-sham operation (Figure 1B). In addition, ARI was significantly less in the iPSC-CM group than the other groups from day 3 onwards (day 17 post-MI) (Figure 2A). Moreover, LVEF was significantly greater in the iPSC-CM group than the other groups between day 3 and day 14 (day 17 and day 28 post-MI) (Figure 2B). These findings indicate that the transplanted cell-sheets of iPSC-CMs generated functional and electrical integration into the acute MI rat heart more rapidly than those of fibroblasts.

In vivo recording of actin-myosin cross-bridge activity in the transplanted iPSC-CMs in the heart

While transplantation of iPSC-CM into the rat infarcted heart was shown to induce functional and electrical recovery, mechanical or functional behavior of each transplanted iPSC-CMs in the infarcted heart remains unclear. Actin-myosin cross-bridge interactions in the transplanted iPSC-CM in the rat infarcted heart was therefore investigated using fast synchrotron small-angle X-ray scattering.

At 4 weeks after the transplantation of iPSC-CM cell-sheets on the surface of the infarcted heart (6 weeks post-MI), the rats were subjected to removal of thoracic wall for the synchrotron study. X-ray diffraction profiles were recorded vertically through the iPSC-CM grafts and infarcted myocardium of the anterior LV wall of the *in situ* beating hearts. It was found that 1,0 and 1,1 equatorial reflections attributable to myosin and actin-myosin lattice

planes typical of cardiac muscle fibres were detected within the iPSC-CM grafts, but not in the infarcted myocardium of the sham-treated rats (Figure 3); albeit reflection intensity was generally much less than that obtained from the remote myocardium. Furthermore, in iPSC-CM hearts cyclic changes in myosin mass-transfer to actin with regular changes in myofilament lattice spacing were evident (Figure 4); similar to that previously reported by us for *in situ* beating rat hearts (20). Importantly, the shift in myosin mass to actin of the iPSC-CMs was synchronous with LV pressure increase during the start of systole on a beat-by-beat basis (Figure 5). The decrease in intensity ratio from end-diastole through early-systole was approximately linearly related to LV pressure development (Figure 5, lower panel). Hence, significant cyclic systolic myosin head transfer to actin filaments, and therefore force-developing cross-bridges were detected within the grafts. Notably, implanted iPSC-CM sheets produced consistent reflections, but the same sheets fresh from culture did not reveal any reflections.

Consistent with the findings in the synchrotron study, myosin and actin were well aligned in the cytoplasm of the Dsred-positive transplanted iPSC-CMs, which were present in the surface of the rat heart, assessed by immunohistolabeling (Figure 6A). In contrast, Dsred-negative native CMs were rarely found in the border and infarct areas which were assessed in the synchrotron study. These findings indicate that the *in situ* X-ray diffraction pattern originated from the transplanted iPSC-CMs, suggesting that regular actin-myosin cross-bridge motion had occurred in the transplanted iPSC-CMs in the rat heart.

Phenotypic and morphological fate of the transplanted iPSC-CM in the heart

Phenotype, morphology and microstructure of the transplanted iPSC-CM, which might be modulated following transplantation into the cardiac tissue, were then histologically analyzed by using immunoconfocal microscopy and electron microscopy. Dsrred-positive transplanted

iPSC-CMs showed myosin-positive sarcomeres at 14 days after transplantation (Figure 6A and B). The sarcomeres consisted of myosin and sarcomeric actin. Although the transplanted iPSC-CMs expressed Cx43 at 14 days, the distribution of Cx43 was scarce, and did not clearly show the typical intercalated disks between the transplanted iPSC-CMs (Figure 6C).

In vitro iPSC-CMs showed typical sarcomeric structures in cardiac myocytes with immature, less dense mitochondria (Figure 6D). On the other hand, clear desmosomes were generated between the iPSC-CMs at 3 days after transplantation, while the mitochondria showed more mature structure compared to that prior to the transplantation. At 7 days, mitochondria showed mature structure, whereas the sarcomeric structure or the number of mitochondria was not as dense as those in the native CMs (Figure 6E and F). This indicates that the transplanted iPSC-CMs by the cell-sheet method might have established electrical/mechanical integrity with the native heart. In addition, maturity in the structure and functionality of the iPSC-CMs progressed after the transplantation into the heart.

DISCUSSION

We demonstrated here that the amount of VEGF and HGF released by iPSC-CMs was not significantly different from that of the same number of fibroblasts, *in vitro*. Transplantation of the iPSC-CM cell-sheets of mouse origin into the nude rat heart that was subjected to MI better preserved LV function and ARI, compared to that of the fibroblasts. Daily electrical mapping of the heart surface uncovered that transplantation of the iPSC-CM induced multiple ectopic excitations over the cell-sheet implanted area for the initial 2 days, and subsequently ectopic excitations disappeared. In *in vivo* synchrotron radiation small-angle scattering studies, the transplanted iPSC-CMs displayed regularly contracting actin-myosin cross-bridge interactions, similar to that recorded in the native cardiomyocytes of the remote myocardium of the same hearts. Immunohistologically, the transplanted iPSC-CMs, which were equipped with myosin-positive sarcomeres in the cytoplasm, formed Cx43-gap-junction with the native cardiomycytes, while electronmicroscopically, the transplanted iPSC-CMs were equipped with immature sarcomeres and mitochondria, compared to the native cardiomyocytes.

The mechanisms underlying the global functional recovery by iPSC-CM transplantation include 1) that transplanted iPSC-CMs survived and showed synchronized contraction *in vivo* as proven by the diffraction analyses, 2) that transplanted iPSC-CMs were equipped with fully developed sarcomeres *in vivo* and these cells might connect with the recipient myocardium, and 3) that there is functional integration of the transplanted iPSC-CMs into the native myocardium to produce direct mechanical contribution to cardiac function. The direct effects of the transplanted cells were studied chiefly by histological assessment of the excised cardiac tissues, which were examined for the presence and integration of the transplanted cells into the native cardiac tissue, but not the functionality of the transplanted cells. For the first time, *in vivo* scans dissected contractile motion of the

CT-1353 Cell Transplantation Early Epub; provisional acceptance 12/04/2014

transplanted cells by X-ray diffraction techniques using synchrotron radiation. Only X-ray diffraction using synchrotron radiation is able to detect rapid transient shifts in myosin mass most likely attributable to strong cross-bridge formation from relatively few muscle fibres within small regions (0.2 mm x 0.2 mm) (12,20). Myosin mass transfer in the first phase of systole in normal myocardial fibres is directly correlated with global LV force development (13). This feature has enabled us to investigate cardiomyocyte function within pin point regions of the graft, the infarct-borderzone and infarct-remote myocardium in heart failure rats. In this study, contractile motion of the Dsred-labeled iPSC-CMs was clearly dissected from the native cardiomyocytes by the synchrotron study, as the cells were transplanted as a sheet form on the heart surface. In the absence of living native cardiomyocytes beneath the graft it is reasonable to conclude that strong cross-bridge formation of the iPSC-CMs contributed to force development, albeit much reduced compared to remote myocardium. In addition, electrical and functional integration of the transplanted iPSC-CMs in the heart was revealed by electrical mapping and echocardiography, supplemented with histological studies, indicating that contraction of each transplanted iPSC-CMs was transferred into the native cardiac motion, at least in part, contributing to the functional recovery of MI heart.

Other possible mechanisms underlying the functional recovery by the transplantation of iPSC-CM cell-sheets might include "paracrine effects" of the transplanted cells on the native heart (19). In fact, this study revealed that the known paracrine factors, such as VEGF or HGF, were released *in vitro* from the iPSC-CMs as from the fibroblasts, while fibroblasts were proven here not to be differentiated into functional cardiomyocytes after transplantation into the heart. Of note, functional recovery was produced in the iPSC-CMs-transplanted hearts but not in the fibroblast-transplanted hearts, despite similar release of the paracrine factors between those two cell-sources. Although these data would be insufficient to determine the magnitude of the "paracrine effects" by the iPSC-CMs therapy, it is suggested

that functional recovery by the iPSC-CMs transplantation might be chiefly caused by mechanical effects of the transplanted cells, and partly by the paracrine effects. Further basic studies are warranted for magnitude and/or durability of paracrine effects by this treatment.

The transplanted graft was integrated into the cardiac tissue beneath the epicardial layer, in particular, the epicardial layer of the infarct and infarct-border territory in this study. In contrast, it seemed that integration of the transplanted cells crossing the epicardium was less prominent in the remote myocardium from the infarct territory (data not shown). We thus consider that integration of the cell-sheet was determined by the microenvironment of the native cardiac tissue and that ablation of the epicardium prior to the cell-sheet transplantation may enhance the integration of the cell-sheet graft (10). In addition, thorough immunohistolabelling and electron microscopy studies showed abundant expression of connexin43 in the graft but rarely identify the gap junction formation between the graft and the native tissue. We consider that presence of a few gap junctions might be enough to transfer electrical current from the native tissue to the grafted cells.

In this study, the transplanted iPSC-CMs showed an "immature" structure, which was not equipped with dense sarcomeric structure and mitochondrial arrangement, as shown in the immunohistolocial and electron microscopy analysis. This was also evident in the lower reflection intensities obtained from sheet-derived CMs compared to native remote myocardium. Importantly, this study indicates that maturity of iPSC-CMs may progress after transplantation into the heart, though quantitative analysis of the "maturity" of the transplanted cells is needed. The functionality of each transplanted iPSC-CMs, in particular its contractility, is the most important factor in determining the therapeutic effects of this treatment. We also showed that the maturity of *in vitro* differentiated iPSC-CMs is variable according to the origin, the cell-line and the culture protocol, and therefore specific regimens used in culture protocols, such as mechanical stretching in the cell-preparation, mimicking the

in vivo environment, might be useful in enhancing the maturation *in vitro* (4,23). One can consider that cell-cell connections between the "immature" cardiomyocytes transplanted into the LV and the native LV cardiomyocytes is likely to produce electrical instability in the LV myocardium resulting in the induction of ventricular arrhythmias. In fact, multiple ectopic excitations appeared in the cell-transplanted area and gradually decreased. Possible causes of the prominent occurrence of premature ventricular contractions in the iPSC-CMs-treated animals would include ectopic excitation directly produced by the transplanted and integrated "immature" iPSC-CMs, or macro/micro re-entries generated by cell transplantation-induced myocardial heterogeneity (1). Although this study failed to dissect the exact cause of the premature contraction, we consider that heterogeneity in the native cardiac tissue would be the main cause, since frequency of the premature contractions was stable for 7 days despite the progressive electrical integration of the graft during this period as in the Figure 1A. While it is unclear that maturation of the transplanted iPSC-CMs is associated with the progressive electrical stability in the LV myocardium in this study, more efficient culture-protocols to enhance maturity of iPSC-CMs, and thereby maximize the therapeutic effects and minimize the arrhythmogenicity of this treatment warrant further investigation.

A limitation of this study may be that we used different species for the iPSC origin and the recipient animal. Interspecies differences may influence functional and electrical integration of the transplanted cells into the recipient native heart. However, the mouse and rat share important proteins related to cell-cell connections and sarcomere structure in the heart (18). The data here therefore are unlikely to be affected by a use of such a xeno-transplantation model. Another limitation could be use of a single iPSC cell-line. As it has been shown that the cell-line is one of the important variable factors that determines the fundamental behavior of iPSCs and their derivatives (22), further studies are warranted to establish an efficient culture protocol to produce the cells that have a consistent quality

CT-1353 Cell Transplantation Early Epub; provisional acceptance 12/04/2014